Modeling nitrogen plasmas produced by intense electron beams

J. R. Angus, D. Mosher, S. B. Swanekamp, P. F. Ottinger, J. W. Schumer, and D. D. Hinshelwood

---

Articles you may be interested in

Intense electron-beam ionization physics in air
Physics of Plasmas **10**, 3758 (2003); 10.1063/1.1600737

Consistent multi-internal-temperature models for vibrational and electronic nonequilibrium in hypersonic nitrogen plasma flows
Physics of Plasmas **22**, 043507 (2015); 10.1063/1.4917338

Cross Sections for Electron Collisions with Nitrogen Molecules
Journal of Physical and Chemical Reference Data **35**, 31 (2006); 10.1063/1.1937426

Simulation of charged-particle beam transport in a gas using a hybrid particle-fluid plasma model
Physics of Plasmas **1**, 764 (1994); 10.1063/1.870768

Evidence of nuclear fusion neutrons in an extremely small plasma focus device operating at 0.1 Joules
Physics of Plasmas **24**, 082703 (2017); 10.1063/1.4989845

A laboratory study of the reactions of N^+, N_2^+, N_3^+, N_4^+, O^+, O_2^+, and NO^+ ions with several molecules at 300 K
The Journal of Chemical Physics **69**, 308 (1978); 10.1063/1.436354

Modeling nitrogen plasmas produced by intense electron beams

J. R. Angus,[1] D. Mosher,[2] S. B. Swanekamp,[1] P. F. Ottinger,[2] J. W. Schumer,[1] and D. D. Hinshelwood[1]

[1]*Plasma Physics Division, Naval Research Laboratory, Washington, DC 20375, USA*
[2]*Independent contractors for NRL through Engility, Inc., Alexandria, Virginia 22314, USA*

A new gas–chemistry model is presented to treat the breakdown of a nitrogen gas with pressures on the order of 1 Torr from intense electron beams with current densities on the order of $10 \, kA/cm^2$ and pulse durations on the order of 100 ns. For these parameter regimes, the gas transitions from a weakly ionized molecular state to a strongly ionized atomic state on the time scale of the beam pulse. The model is coupled to a 0D–circuit model using the rigid–beam approximation that can be driven by specifying the time and spatial profiles of the beam pulse. Simulation results are in good agreement with experimental measurements of the line–integrated electron density from experiments done using the Gamble II generator at the Naval Research Laboratory. It is found that the species are mostly in the ground and metastable states during the atomic phase, but that ionization proceeds predominantly through thermal ionization of optically allowed states with excitation energies close to the ionization limit. *Published by AIP Publishing.*
[http://dx.doi.org/10.1063/1.4950840]

I. INTRODUCTION

Intense, relativistic–electron beams (REBs) are used to study gas discharges,[1–3] material processing,[4] bremsstrahlung radiation production,[5] and material responses to pulsed energy deposition. The Gamble II (GII) generator[6] at the Naval Research Laboratory is capable of producing ~100 ns pulse–duration REBs with peak energies on the order of 1 MV and peak currents around 800 kA with areas of 40–80 cm^2. This gives peak current densities on the order of $10 \, kA/cm^2$. For many applications, beam transport is achieved by filling the transport region with gases in the 1–Torr pressure range. In these parameter regimes, the nitrogen gas transitions from a weakly ionized molecular state to a strongly ionized atomic state on the time scale of the beam pulse.[2] A detailed gas–chemistry model is presented in this paper for a dynamical description of the nitrogen plasmas produced in such experiments.

Transport of intense REBs is achieved when the gas breaks down to form a plasma that can provide sufficient charge and current neutralization of the beam.[7] The degree of charge and current neutralization required depends on the type of transport needed and on the beam current, I_b, compared to the space–charge–limited current, I_ℓ, and the Alfvèn current, I_A. The initial source of background plasma in the systems of interest is from high–energy beam electrons ionizing the neutral gas particles. Secondary electrons produced in these ionization events are subsequently accelerated by the inductive electric field associated with the net current pulse and further ionize the gas through thermal processes. When the beam and gas parameters are such that the secondary electrons produced in the gas have a mean free path that is short compared to the beam radius, and a collision time that is short compared to the rise time of the beam, the response of the gas is coupled to the field and beam–evolution equations through a local conductivity.

The conductivity is strongly dependent on the mean electron energy in the discharge. The mean energy affects the distribution of excited–energy states of the gas, which can vary strongly for intense beams on the time scale of the pulse duration. The distribution of excited–energy states is referred to as the state of the gas. In the weakly ionized state, where resistivity is set by electron momentum transfer with neutral species, the conductivity scales linearly with the electron density and the mobility has a weak dependence on the electron temperature T_e. However, once the gas becomes highly ionized such that the resistivity is set by momentum transfer with ions rather than neutrals, the conductivity becomes weakly dependent on the electron density and scales with $T_e^{3/2}$. Since the electron temperature is typically set by a balance between Joule heating and inelastic losses to heavy species (hs), a thorough gas–chemistry model that includes all of the important species and reactions is vital for correctly determining the conductivity.

Many past studies of REBs propagating in ~1–Torr nitrogen use simplified gas–chemistry models[8–10] that are based on assumptions that the gas remains weakly ionized and molecular. These models evolve the electron density in time use a local rate equation that includes sources from beam–impact ionization and thermal avalanche and dissociative recombination as a sink. The thermal transport coefficients in these models, which include the electron temperature and momentum exchange, are computed as functions of the local reduced electric field, E/N, where E is the magnitude of the local electric field and N is the number density of the ground state gas species. These coefficients are pre–computed using an electron–energy–distribution function (EEDF) obtained from a two–term Boltzmann solver for a weakly ionized gas where electrons interact with the ground–state gas species only and power balance is assumed.[11] These models are typically referred to as swarm models.

Some of the earliest works using swarm models to describe the breakdown and conductivity of a nitrogen gas due to a pulsed REB are those of McArthur and Poukey.[8,9] They coupled their gas chemistry model to a 2D, electromagnetic model assuming a rigid paraxial beam and illustrated the influence of the radial dependence of the conductivity on the azimuthal magnetic field.[8] Their model was able to reproduce net current measurements within the experimental error for about 90% of the pulse duration from experiments in the 1–20 Torr pressure range with 80–ns pulses and current densities $\sim 1\,\text{kA/cm}^2$. They also obtained qualitative agreement with net current measurements from experiments with 40–ns pulses and peak current densities of about $20\,\text{kA/cm}^2$. However, the agreement with these experiments was not as good compared to the lower current density experiments. The authors comment that the reason for poorer agreement with the experiments at higher current density could be due to the fact that the gas could have a significant population of excited–energy states as well as becoming dissociated.

Another gas–chemistry model that has been utilized in many charged–particle–beam transport studies in gases[2,10,12–14] is the model by Welch *et al.*[10] This model is similar to the one described in Refs. 8 and 9, but includes additional features to account for effects that become important for pressures below 1 Torr. This includes an additional sink of electrons due to run-away that occurs at high E/N values and reduced particle mobility due to strong magnetic fields, where the electron cyclotron frequency becomes large compared to the electron momentum exchange frequency. This model has been implemented in the particle–in–cell (PIC) code LSP[15] for hybrid simulations where the high–energy beam electrons are treated using PIC and the background plasma is modeled as a fluid.

The limitations of using conventional swarm models to describe ~ 1 Torr nitrogen and air (about 80% nitrogen) plasmas produced by REB's with current densities on the order of $10\,\text{kA/cm}^2$ and pulse–widths on the order of $100\,\text{ns}$ are illustrated in Ref. 2. For these parameter regimes, the gas reaches a highly ionized and atomic state. This is demonstrated experimentally using interferometry measurements, which show ionization fractions between 20% and 100% near the end of the pulse. Ionization fractions this high cannot be reached if the gas remains in a molecular state due to

the relatively large dissociative recombination rate of molecular ions compared to three–body recombination and radiative recombination rates for atomic ions.

In an initial attempt at a more physically correct nitrogen plasma model for GII experiments, Strasburg *et al.*[3] extended LSP's swarm model to allow the transition of the gas from molecular to atomic by including some dissociation physics and a time–dependent corona model for handling higher ionization states that become important for current densities $\gtrsim 100\,\text{kA/cm}^2$. This model also uses a Maxwellian EEDF for computing transport coefficients rather than that from the two–term solution, which is more appropriate for the large ionization fractions reached in the experiments. The electron temperature is obtained in this model from a time–dependent electron power equation. Details of this model are given in Ref. 15

The model by Strasburg *et al.* is much more appropriate for the GII parameter regimes than the conventional swarm models described previously. However, this model uses crude expressions for thermal processes. For example, the ionization rate constants used are good for ionization of ionic states, but are not good for ionization of neutral states. The model presented here considers the molecular–atomic transition in much more detail than the one used in Ref. 3 and uses appropriate reaction rates computed from up–to–date cross–section data for the most important molecular and atomic processes. The gas–chemistry model is described in detail in Secs. II and III. This model is then coupled to a 0D–circuit model representative of annular beams, and results using parameters typical for GII experiments are presented in detail.

II. GAS–CHEMISTRY MODEL

The species followed in the gas–chemistry model are listed in Table I. The model contains nine molecular neutral species that include the ground state $N_2(X^1\Sigma)$ along with the four lowest–lying triplet states $N_2(A^3\Sigma, B^3\Pi, W^3\Delta, B'^3\Sigma)$, the three lowest–lying singlet states $N_2(a'^1\Sigma, a^1\Pi, w^1\Delta)$, and the upper triplet state $N_2(C^3\Pi)$. There are three molecular ion species including the ground state $N_2^+(X^2\Sigma)$ and the first two excited states $N_2^+(A^2\Pi, B^2\Sigma)$, all of which are doublet states. The atomic neutral species followed in the model include the ground state $N(^4S^o)$, the two low–lying metastable states that share the same electron configuration as the ground state

TABLE I. Species followed in the gas–chemistry model. All of the molecular–excitation energies listed are with respect to the ground neutral molecular state and similarly for the atomic species with charge state $Z \leq 1$. The energies listed for the atomic ion species with $Z > 1$ are with respect to the ground electronic state of the $Z - 1$ charge state.

Species class	Species state	Excitation energy (eV)
Molecular neutral species (N_2):	$X^1\Sigma, A^3\Sigma, B^3\Pi, W^3\Delta, B'^3\Sigma,$	0, 6.17, 7.35, 7.36, 8.17,
	$a'^1\Sigma, a^1\Pi, w^1\Delta, C^3\Pi$	8.40, 8.55, 8.89, 11.0
Molecular ion species (N_2^+):	$X^2\Sigma, A^2\Pi, B^2\Sigma$	15.6, 16.7, 18.8
Atomic neutral species (N):	$^4S^o, {}^2D^o, {}^2P^o,$	0, 2.39, 2.57,
	$3s\,^4P, 3s\,^2P, 2p^4\,^4P,$	10.42, 10.77, 10.95,
	$3p\,^2S^o, 3p\,^4D^o, 3p\,^4P^o, 3p\,^4S^o,$	11.62, 11.79, 11.87, 12.00,
	$3p\,^2D^o, 3p\,^2P^o, 3s\,^2D, 4s\,^4P,$	12.03, 12.15, 12.37, 12.85,
	$4s\,^2P, 3d\,^2P, 3d\,^4F, 3d\,^4P,$	12.92, 12.96, 12.97, 12.98,
	$3d\,^2F, 3d\,^4D, 3d\,^2D$	12.99, 13.01, 13.02
Atomic ion species with Z = 1 (N^+):	$^3P, {}^1D, {}^1S$	14.5, 16.4, 18.6
Atomic ion species with Z > 1 ($N^{(Z)}$):	$2 \leq Z \leq 7$	29.6, 47.5, 77.5, 97.9, 552, 667

$(1s^2 2s^2 2p^3)$, $N(^2D^o, {}^2P^o)$, and the first 18 optically allowed states. For the singly ionized atomic ion species, the states considered are the ground state $N^+(^3P)$ and the two low–lying metastable states that share the same electron configuration as the ground state $(1s^2 2s^2 2p^2)$, $N^+(^1D, {}^1S)$. The ground electronic states of ionized atomic nitrogen with charge state $Z > 1$ are also contained in the model. None of the $Z > 1$ species have low–lying electronic levels that share the same ground–state–electron configuration.

The parameter regimes of interest permit the use of several simplifying assumptions to reduce the reaction processes retained in the gas–chemistry model. First, the pressures of interest ($\gtrsim 1$ Torr) are high enough that the system is highly collisional and the local approximation is valid. Second, the ionization state of the gas quickly reaches a high enough level that (1) the EEDF is Maxwellian, and (2) the system of rate equations for the different species are dominated by electron–impact reactions and other processes, such as heavy–heavy reactions and radiative transitions, can be ignored. Lastly, while the time scales of interest (~ 100 ns) are long enough that the electrons are collisionally relaxed, they are short enough that heavy particle heating can be ignored and the hydrodynamic motion of the plasma via ambipolar diffusion and J × B forces can be neglected.

There are two different groups of electrons that contribute to the system of rate equations—high–energy beam electrons and a thermal background. The different types of reactions considered for both of these groups of electrons retained in the gas–chemistry model are described in Subsections II A–II C.

A. Thermal reactions with molecular species

The specific reactions involving thermal electrons with molecular nitrogen included in the gas–chemistry model are listed in Table II. All electronic excitation cross sections for collisions with the ground state $N_2(X^1\Sigma)$ are taken from Itikawa.[16]

TABLE II. Thermal reactions with molecular nitrogen species.

Reaction	References
Electronic excitation/quenching: $e + N_2(X^1\Sigma) \Longleftrightarrow e + N_2(j \neq X^1\Sigma)$	16
Dissociation to neutrals: $e + N_2(i) \Rightarrow \begin{cases} e + 2N(^4S) \\ e + N(^4S) + N(^2D) \\ e + N(^4S) + N(^2P) \\ e + 2N(^2D) \end{cases}$	16, 17, 20–22
Direct ionization: $e + N_2(i) \Rightarrow 2e + N_2^+(j)$	16, 29
Dissociative ionization: $e + N_2(X^1\Sigma) \Rightarrow \begin{cases} 2e + N(^4S) + N^+(^3P) \\ 2e + N(^2D) + N^+(^3P) \end{cases}$	16, 17, 20
Dissociative recombination: $e + N_2^+(i) \Rightarrow \begin{cases} e + N(^4S) + N(^2D) \\ e + N(^4S) + N(^2P) \\ e + 2N(^2D) \end{cases}$	32

All electronic de–excitation processes are computed using detailed balance. The dominant contribution to collisional dissociation of $N_2(X^1\Sigma)$ to neutral products occurs through the predissociation of several different electronic states with energies exceeding 11 eV (Ref. 17) (note that the dissociation potential to form two $N(^4S)$ states is 9.75 eV). In this work, dissociation of $N_2(X^1\Sigma)$ is considered to occur through the electronic states $N_2(E^3\Sigma, a''^1\Sigma, b^1\Pi, b'^1\Sigma,$ and $c'^1\Sigma)$.[18] The excitation cross sections for the $E^3\Sigma$ and $a''^1\Sigma$ states are taken from Ref. 16, and the cross section for the sum of the numerous singlet levels is taken from Ref. 17 (also see Ref. 19). These cross sections are used in the computation of power loss from the ground state. The cross sections used for the atomic density evolution equations due to the different dissociation channels from the ground state are taken from Ref. 20. Cross sections for electron–impact dissociation from the electronically excited states of N_2 are calculated using the weighted–total–cross–section (WTCS) method described in Refs. 21 and 22. These calculations are carried out using a Morse potential function with spectroscopic data from Ref. 23 and using the potential curves in Ref. 24.

It is well–known that vibrational kinetics plays an important role in many different low–temperature nitrogen discharges,[25–28] where the electron temperature is on the order of 1 eV. The importance of rotational modes occurs for sub–eV temperatures. However, the electron temperature during the molecular phase for systems of interest here is on the order of 10 eV or greater where electron impact excitation, dissociation, and ionization play a much more important role. For these reasons, the rotational and vibrational distributions of the molecular states are not considered. Each of the molecular species in the model are essentially assumed to be in the ground rotational and vibrational states.

The cross sections for state–to–state ionization from each electronic state of N_2 to form each of the electronic states of N_2^+ are obtained using the processes discussed by Kosarim *et al.*,[29] rescaled so that the total cross section for ionization from the ground state has the same peak as the total cross section for direct ionization given by Itikawa.[16] The potential energy curves needed for these computations are computed using the Rydberg–Klein–Rees (RKR) method discussed in Refs. 24 and 30 with the spectroscopic data taken from Ref. 23. Only ionization channels that correspond to a single electron transition are retained. For example, the ionization channel $e + N_2(A^3\Sigma) \Rightarrow 2e + N_2^+(X^1\Sigma)$ requires two–electron transitions and is therefore not considered.[31]

Dissociative recombination for molecular nitrogen ions is described using the rate constant obtained from Ref. 32

$$k_{dr} = 5.85 \times 10^{-8}/T_e^{0.30} \, \text{cm}^3/\text{s}, \tag{1}$$

where T_e is in eV. The branching ratios for the fragments $N(^4S) + N(^2D) : N(^2P) + N(^2D) : 2N(^2D)$ are taken to be $0.37{:}0.11{:}0.52$[32] for all electron temperatures. The rate constant for dissociative recombination of molecular ions is several orders of magnitude larger than the other recombination mechanisms in moderate pressure discharges.[33] Neglecting other recombination mechanisms for molecular ions, such as radiative and three–body recombination, can be justified

using characteristic rate constants for these processes and by considering typical parameters of interest. A characteristic rate constant for radiative recombination is $\alpha = 2.7 \times 10^{-13}/\sqrt{T_e}$ cm^3/s (Ref. 34) and that for three–body recombination is $k_{3b} = n_e \times 9 \times 10^{-27}/T_e^{4.5}$ cm^3/s, where n_e is in units of 1/cm^3. For order unity electron temperatures and a fully ionized 1–Torr plasma ($n_e \approx 10^{16}$ cm^3/s), the characteristic e–folding time for recombination through dissociation, radiation, and three–body processes are approximately 5 ns, 100 μs, and 1 μs, respectively.

B. Thermal reactions with atomic species

The thermal reactions with the atomic species included in the gas–chemistry model are given in Table III. The cross sections for transitions between all electronic states of neutral atomic nitrogen are taken from the recent B–spline, R–Matrix calculations by Wang *et al.*[35] The metastable excitation cross sections from these calculations are in good agreement with the commonly used calculations of Berrington *et al.*,[36] but are from much more detailed calculations and do a better job of resolving the resonances. Cross sections for transitions between the ground and metastable states of N^+ are taken from Ref. 37, which are also used in Ref. 38.

State–to–state ionization from the ground and metastable electronic states of neutral atomic nitrogen into the ground and metastable states of singly ionized atomic nitrogen are computed using the binary–encounter Bethe (BEB) model described by Kim *et al.* in Ref. 39. These cross sections are in good agreement with both the experimental data from Brook *et al.*[40] and the recent computations by Wang *et al.*[35] The auto–ionization cross sections of the metastable states $N(^2D)$ and $N(^2P)$ are included in the total ionization cross sections for these states. The ionization of a specific electron state of N into a specific electronic state of N^+ is obtained in this method by weighting the cross section by the ratio of the statistical weight of the ion's electronic state to the sum of the statistical weights of all ion states considered.[39]

Cross sections for the ionization of the optically allowed atomic states of neutral nitrogen and all ionic states are computed using the empirical formula given by Lotz,[41,42] which is a function of the ionization potential and the number of electrons in the shell being ionized and contains fitting parameters to match experimental data for ionization of different species. Cross sections for ionization of the optically allowed neutral states are computed using the fitting parameters given by Lotz for $N(^4S^o)$. Cross sections for ionization from a specific optically allowed neutral state into a specific

TABLE III. Thermal reactions with atomic nitrogen species.

Reaction	References
Electronic excitation/quenching:	
$e + N(i) \Longleftrightarrow e + N(j > i)$	35, 36
$e + N^+(i) \Longleftrightarrow e + N^+(j > i)$	37
Ionization/3–body recombination:	
$e + N(i) \Longleftrightarrow 2e + N^+(j)$	39, 40, 42
$e + N^+(i) \Longleftrightarrow 2e + N^{(2)}$	42
$e + N^{(z)} \Longleftrightarrow 2e + N^{(z+1)}$	42

electronic level of N^+ are obtained using the same weighting procedure with the statistical weights of the ions used by Kim *et al.*[39] for the state–to–state ionization of the ground and metastable states. Rate constants for ionization from the optically allowed states computed using this method are in very good agreement with those computed using much more sophisticated models.[43]

The dominant atomic–ion recombination mechanism for the parameter regimes of interest is three–body recombination. Although this processes was estimated in Subsection II A to occur on a time scale that is about a factor of 10 larger than the 100–ns time scales of interest, this processes is retained for atomic–ion species in the gas–chemistry model for completeness and since reaction rates for these processes can be readily obtained with minimal effort using the principles of detailed balance.

C. Beam–impact reactions

Particle sources and sinks due to beam–impact processes are included in the model using the beam stopping power, $d\varepsilon_b/dx$, along with the energy needed to produce an electron–ion pair, W, and the production efficiencies η as presented in Refs. 38 and 44. Using this formalism, the total source of thermal electrons due to beam–impact reactions is written as

$$\left.\frac{\partial n_e}{\partial t}\right|_b = n_b v_b \sum_i \frac{1}{W_i}\left.\frac{d\varepsilon_b}{dx}\right|_i, \qquad (2)$$

where $n_b v_b$ is the beam flux and the sum is taken over all heavy gas species i. The electron stopping power due to collisions with heavy species i with density n_i can be written as $d\varepsilon_b/dx|_i = n_i L_i$ where L_i is known as the loss function. The loss function for beam electrons with speed $v_b = c\beta_b$ in a gas i can be defined using the Bethe formula as[45]

$$L_i = 4\pi m_e c^2 Z_i r_e^2 \frac{\ln\left[2m_e c^2 \beta_b^2 \gamma_b^2/I_i\right] - \beta_b^2}{\beta_b^2}, \qquad (3)$$

where $m_e c^2 = 0.511$ MeV is the electron rest energy, $r_e = 2.818 \times 10^{-13}$ cm is the classical electron radius, I_i is the mean excitation potential, which is about 85 eV for nitrogen, and Z_i is the number of electrons per particle of heavy species i. For example, $Z_N = 7$ for atomic nitrogen and $Z_{N2} = 14$ for molecular nitrogen. Kinetic studies of steady–state, high–energy–electron beams in nitrogen have shown W_i is approximately constant for beam energies between 1 keV and 1 MeV with $W_{N2} = 36.5$ eV for molecular nitrogen,[44] $W_N = 31$ eV in neutral atomic nitrogen, and $W_{N+} = 71$ eV in singly ionized atomic nitrogen.[38]

The source terms for different excited states of molecules and atoms due to beam–impact reactions can be described similarly to Eq. (2) using production efficiencies, which are also approximately constant for beam energies between 1 keV and 1 MeV. The production efficiency for a given excited state is defined as the number of such states produced for every electron–ion pair produced. The efficiencies used in our model are given in Table IV. The values for beam–impact reactions with molecular nitrogen in Table IV are an average

TABLE IV. Beam–impact reactions included in gas–chemistry model along with production efficiencies.

Reaction	η
Molecular reactions (W = 36.5 eV)	
$e_b + N_2(X^1\Sigma) \Rightarrow e_b + N_2(A^3\Sigma, B^3\Pi)$	0.163, 0.144
$e_b + N_2(X^1\Sigma) \Rightarrow e_b + N_2(W^3\Delta, B'^3\Sigma)$	0.108, 0.029
$e_b + N_2(X^1\Sigma) \Rightarrow e_b + N_2(a'^1\Sigma, a^1\Pi)$	0.027, 0.077
$e_b + N_2(X^1\Sigma) \Rightarrow e_b + N_2(w^1\Delta, C^3\Pi)$	0.03, 0.055
$e_b + N_2(i) \Rightarrow e_b + N(^4S) + N(^2D)$	0.452
$e_b + N_2(i) \Rightarrow e_b + e + N_2^+(X^2\Sigma)$	0.338
$e_b + N_2(i) \Rightarrow e_b + e + N_2^+(A^2\Pi)$	0.353
$e_b + N_2(i) \Rightarrow e_b + e + N_2^+(B^2\Sigma)$	0.117
$e_b + N_2(i) \Rightarrow e_b + e + N(^4S) + N^+(^3P)$	0.097
$e_b + N_2(i) \Rightarrow e_b + e + N(^2D) + N^+(^3P)$	0.097
$e_b + N_2(i) \Rightarrow e_b + 2e + 2N^+(^3P)$	0.0045
Neutral atomic (W = 31 eV)	
$e_b + N(^4S) \Rightarrow e_b + N(^2D)$	1.55
$e_b + N(^4S) \Rightarrow e_b + N(^2P)$	0.35
$e_b + N(i) \Rightarrow e_b + e + N^+(^3P)$	1.00
Atomic ion (W = 71 eV)	
$e_b + N^+(i) \Rightarrow e_b + e + N^{(2)}$	1.00

of those for a 1 keV beam and a 1 MeV beam given in Ref. 44. Values for interactions with atomic nitrogen are taken from Ref. 38. Beam impact dissociation and ionization reactions with the excited states are also included in the model. For simplicity, the production efficiencies for these reactions are taken to be the same as those with the ground states. Also for simplicity, it is assumed that all dissociation to neutral products result in the production of one ground and one $N(^1D)$ state and that dissociative–ionization reactions result in $N(^4S) + N^+(^3P)$ and $N(^2D) + N^+(^3P)$ with equal efficiencies.

The beam–impact source term given in Eq. (2) accounts for both direct beam–impact ionization, which produces intermediate–energy secondaries, as well as ionization due to the secondaries as they relax to thermal energies. This effect is captured in Refs. 8 and 9 using the ionization cross section scaled by an enhancement factor. This is valid as long as the spatial scales of the beam are large compared to the secondary mean free path and the time scales associated with the beam are long compared to the secondary relaxation time. As an example, ionization due to a 1 MeV beam electron produces a secondary with an average energy of about 65 eV.[44] This secondary has $\sim$1 mm mean free path and a collision time less than 1 ns in 1–Torr molecular nitrogen. Since 65 eV is much greater than the 15.6 eV ionization potential of $N_2(X^1\Sigma)$, these secondaries will produce additional ionization as they relax. This is valid for our problem where the beam thicknesses is on the order of 1 cm and the beam pulse duration is on the order of 100 ns.

III. GOVERNING EQUATIONS

A general formalism for the system of rate equations governing the heavy species densities is obtained by assuming that the divergence of spatial fluxes is negligible with respect to local sources and sinks and can be written as

$$\frac{\partial n_i}{\partial t} = \sum_{j\neq i} \left[n_b v_b \left(n_j \frac{L_j}{W_j} \sum_{m=1}^{m_{\max,j}} i_{j,i}^m \eta_{j,i}^m - n_i \frac{L_i}{W_i} \sum_{m=1}^{m_{\max,i}} \eta_{i,j}^m \right) \right. $$
$$\left. + n_e \left(n_j \sum_{l=1}^{l_{\max,j}} i_{j,i}^l k_{j,i}^l - n_i \sum_{l=1}^{l_{\max,i}} k_{i,j}^l \right) \right]. \quad (4)$$

In the above equation, the first two terms represent the net source of density for heavy species i due to beam–impact reactions and the last two terms represents the net source due to thermal reactions. The outer sum is over all species $j \neq i$. The inner sum of the first and third terms is over all reactions with species j that result in the production of species i and the inner sum of the second and fourth terms is over all reactions with species i that results in a loss of species i. The term $i_{j,i}^m$ is the multiplicity of states i produced in reaction m (or l) with species j. It is either one or two, the latter of which is the case for certain dissociation reactions. The beam–impact reaction rates scale with the beam flux, $n_b v_b$, and transitions between state j and i are described using the loss function, L_j, the energy needed to produce an electron–ion pair, W_j, and the production efficiencies, $\eta_{i,j}^m$.[38,44] The thermal reactions rates scale with background electron density, n_e, and the transition between species i and j due to thermal process l are described using rate constants, $k_{i,j}^l$.

The rate constant for inelastic process l that corresponds to the transition from state i with density n_i to state j with density n_j described by the cross section $\sigma_{i,j}^l$ is

$$k_{i,j}^l = \sqrt{\frac{2e}{m_e}} \int_0^\infty \varepsilon \sigma_{i,j}^l F_0 d\varepsilon, \quad (5)$$

where ε is the electron energy in eV and F_0 is the EEDF normalized such that $\int_0^\infty \sqrt{\varepsilon} F_0 d\varepsilon = 1$. All transport coefficients in the gas–chemistry model are computed using a Maxwellian EEDF

$$F_0 = \frac{2}{\sqrt{\pi} T_e^{3/2}} \exp\left(-\frac{\varepsilon}{T_e}\right), \quad (6)$$

where $T_e = 2\int_0^\infty \varepsilon^{3/2} F_0 d\varepsilon /3$ is the electron temperature in eV.

The inverse cross section for excitation collisions, also known as superelastic collisions, can be calculated using the principles of detailed balancing. Rate constants for superelastic collisions can be computed in terms of the forward rate constant when the EEDF is a Maxwellian as

$$k_{j,i}^l = \frac{g_i}{g_j} k_{i,j}^l \exp\left(\frac{U_{i,j}^l}{T_e}\right), \quad (7)$$

where g_j is the statistical weight of the excited species, g_i is the statistical weight of the species after the quenching collisions, and $U_{i,j}^l$ is the potential energy for the transition from the excited state i to state j described by the rate constant $k_{i,j}^l$ computed using Eq. (5). For three–body recombination with ions of charge state Z, the inverse rate constant is

$$k_{j,i}^Z = n_e \frac{1.66 \times 10^{-22}}{T_e^{3/2}} \frac{g_i^{Z-1}}{g_j^Z} k_{i,j}^{Z-1} \exp\left(\frac{U_{i,j}^{Z-1}}{T_e}\right), \quad (8)$$

where $k_{i,j}^{Z-1}$ is the ionization rate constant for the transition of state i with charge $Z-1$ to state j with charge Z. A neutral can also act as the third body, but the rate constant is three to four orders of magnitude smaller than that when the electron acts as the third body.[46]

The background electron density is obtained from charge conservation

$$n_e = \sum_Z Z n^{(Z)}, \qquad (9)$$

where $n^{(Z)}$ is the total density of ions with charge state Z. The equation governing the electron temperature is obtained by assuming that spatial gradients are weak in comparison to local heat sources and sinks and is given by

$$\frac{\partial}{\partial t}\left(\frac{3}{2}n_e T_e\right) = P_b + \mathbf{J}_p \cdot \mathbf{E} - \sum_{i \in \text{hs}}\sum_{l=1}^{l_{\max_i}} Q_{i,j}^l, \qquad (10)$$

where P_b is the source of energy density due to beam–impact heating, $\mathbf{J}_p = -en_e\mathbf{V}_e$ is the plasma current density, and the $Q_{i,j}^l$ terms represent the electron energy exchanges to inelastic processes. The outer sum in the last term is over all heavy species (hs) and the inner sum is over all inelastic processes with heavy species i. It is assumed that energy exchanges due to elastic collisions are negligible with respect to inelastic processes.

The energy density exchange term due to inelastic process l for the transition $i \rightarrow j$ with potential $U_{i,j}^l$ can be written as

$$Q_{i,j}^l = n_e U_{i,j}^l k_{i,j}^l n_i. \qquad (11)$$

The above equation results from assuming that electrons are scattered isotropically in an inelastic event. Note that $U_{i,j}^l$ is negative for reverse processes. Energy loss to recombination processes is assumed to be $3T_e/2$.

The source of energy density from beam–impact reactions in Eq. (10) can be approximated using the stopping power and can be written as

$$P_b = n_b v_b n_a L_N, \qquad (12)$$

where L_N is the loss function with atomic nitrogen defined using Eq. (3) and $n_a = 2\sum_{i=\text{ms}} n_i + \sum_{i=\text{as}} n_i$ is the locally conserved total atom density. It should be noted that Eq. (12) is an overestimate of the thermal energy source from beam–impact processes since some of the energy lost by the beam goes into raising the gas to a higher internal–energy state. However, as will be shown below, for our parameter regime this term is small compared to the Joule heating term associated with the plasma return current, which is given by Ohm's law in the highly collisional limit as

$$\mathbf{J}_p = \sigma_p \mathbf{E}, \qquad (13)$$

where $\sigma_p = n_e e^2/(m_e \nu_{\text{mom}})$ is the plasma conductivity and the total momentum–transfer frequency is given by $\nu_{\text{mom}} = \nu_{en} + \nu_{ei}$ with ν_{en} the electron–neutral momentum–transfer frequency and ν_{ei} the electron–ion momentum–transfer frequency. The Lorentz force is ignored in Eq. (13) by assuming that the current neutralization is good enough for the systems of interest that $\Omega = eB/(m_e c) \ll \nu_{\text{mom}}$.

The momentum–transfer frequency with neutrals can be written as $\nu_{en} = e/(m_e \mu_{\text{en}})$, where the mobility μ_{en} is defined by[11]

$$\mu_{\text{en}} = -\frac{1}{3}\sqrt{\frac{2e}{m_e}}\int_0^\infty \frac{\varepsilon}{\sum_i n_i \sigma_i^{\text{mom}}}\frac{\partial F_0}{\partial \varepsilon}d\varepsilon. \qquad (14)$$

In the above equation, $\sigma_i^{\text{mom}} = \sigma_i^{\text{elm}} + \sum_l \sigma_i^l$ is the total momentum transfer cross section with neutral species i, which is the sum of the elastic–momentum–transfer cross section, σ_i^{elm}, and all inelastic cross sections, σ_i^l. The elastic–momentum–transfer cross sections for all of the neutral molecular species are assumed to be equivalent to that for the ground state taken from Ref. 16. For the atomic neutral species, the elastic–momentum–transfer cross sections are taken from Ref. 35, which provides σ_i^{elm} for the ground and metastable states and the elastic cross sections for all higher–energy states. It is reasonable to assume that the elastic cross sections are a good approximation of σ_i^{elm} for the energy range of interest. These cross sections display a strong dependence on the principle quantum number as discussed in Refs. 47 and 48.

The electron–ion momentum–transfer time is given by Spitzer[49] as $\nu_{ei} = \alpha_0/\tau_{ei}$, where

$$\tau_{ei} = 3.44 \times 10^5 \frac{T_e^{3/2}}{\bar{Z} n_e \lambda_{ei}}, \qquad (15)$$

is the electron–ion collision time and α_0 is the Spitzer factor that depends on the average charge state of the ions. In Eq. (15), τ_{ei} has units of seconds, T_e is in eV, n_e is in 1/cm^3, λ_{ei} is the Coulomb logarithm for electron-ion collisions, and $\bar{Z}$ is the average charge state of the ions defined as

$$\bar{Z} \equiv \frac{1}{n_e}\sum_{Z=1}^{Z_{max}} Z^2 n^{(Z)}. \qquad (16)$$

The Spitzer factor accounts for the effects of electron–electron relaxation on electron–ion momentum transfer. This parameter has the value $\alpha_0 = 0.51$ for $\bar{Z} = 1$ and reduces $\alpha_0 = 3\pi/32$, which is the Lorentz value, in the limit where $\bar{Z} \rightarrow \infty$.

In general, modeling the systems of interest requires a coupled system of equations governing the gas chemistry, the electric and magnetic fields, and the beam–electron orbits. However, the charge and current neutralization in many GII experiments is sufficient to allow ballistic–like transport of the beam electrons. This is supported experimentally by x–ray imaging from both the entrance and exit planes of the transport region.[2] This permits the use of the rigid–beam approximation[8,9,50] where the beam–electron orbits are assumed to be perfectly ballistic. In this approximation, the beam enters the gas–chemistry model as a source of background species and energy and enters Maxwell's equations as a source of magnetic and electric fields, but self–consistent beam orbits are ignored.

A 0D–inductive circuit model can be derived using the rigid–beam approximation along with several other simplifying assumptions. The gas–filled transport cell walls are assumed to be a perfectly–conducting cylinder with radius r_w and axial length z_w. A cold, rigid beam is assumed so that all beam electrons enter the cell moving in the z-direction. It is assumed that the system is both axially symmetric ($\partial/\partial\phi = 0$) and axially invariant ($\partial/\partial z = 0$). Axial uniformity can be assumed when the transit time of the beam electrons across the gap z_w is short compared to the characteristic time scale associated with the beam pulse[9] and the beam–electron energy losses are small. Charge neutralization typically occurs on a sub–nanosecond time scale,[2,8] which is much shorter than the 100–ns rise times of interest, and the electric field driving the return current is dominated by the inductive component. Using the symmetry assumptions mentioned above, the inductive electric field can be obtained from Faraday's law ($\nabla \times \mathbf{E} = -\partial\mathbf{B}/\partial t/c$) as

$$E_z(r,t) = \frac{-1}{c}\frac{\partial}{\partial t}\int_r^{r_w} B_\theta(r,t)\,dr, \tag{17}$$

where the perfectly conducting boundary condition at the wall radius ($E_z(r = r_w, t) = 0$) is used.

The azimuthal magnetic field in Eq. (17) can be expressed in terms of the total current density, $J = (\mathbf{J}_b + \mathbf{J}_p) \cdot \hat{\mathbf{z}}$, using Ampere's law in the limit where the displacement current can be ignored ($\nabla \times \mathbf{B} = 4\pi\mathbf{J}/c$). For simplicity, J is taken to be uniform between radii r_1 and r_2 and zero otherwise. For a uniform beam profile between r_1 and r_2, the assumption that the plasma return current is uniform requires the electric field also be uniform between r_1 and r_2. This is true when the inductance per unit length from the outer edge of the beam at r_2 to the wall at r_w is much greater than the inductance per unit length across the beam/plasma channel. In this limit, $E_z(r \le r_2)$ can be expressed as

$$E_z(r \le r_2, t) = -L_z'\frac{dI_{\text{net}}}{dt}, \tag{18}$$

where $L_z' = 2\ln(r_w/r_2)/c^2$ is the inductance per unit length from r_2 to r_w and $I_{\text{net}} = \pi(r_2^2 - r_1^2)J$ is the net current. For thin beams such that $\Delta r_b = r_2 - r_1 \ll r_b$, the assumption that L_z' above the beam is much larger than that across the beam holds when $\Delta r/(2r_1) \ll \ln(r_w/r_2)$. This assumption is marginally satisfied for the beams of interest that have a radius of 7 cm and about a 1–cm thickness.

Equation (18) can be rewritten as an expression for the beam current density using Ohm's law

$$\frac{d}{dt}J_p + \nu J_p = -\frac{d}{dt}J_b, \tag{19}$$

where $\nu = 1/(L_z'A_b\sigma_p)$ and $A_b = \pi(r_2^2 - r_1^2)$ is the beam area. Equation (19) is the 0D–inductive circuit model governing the plasma current density in terms of the time–dependent beam–current density and time–dependent plasma conductivity profiles. It is worth mentioning that $1/\nu$ is the L/R time of the circuit where $L = L_z'\ell_z$ is the circuit inductance and $R = \ell_z/(A_b\sigma_p)$ is the circuit resistance.

IV. SIMULATION RESULTS

Simulation results are presented in this section using beam parameters and time profiles that are typical of experiments using the GII generator to drive annular electron beams.[2] The plasma return current is obtained from Eq. (19) with the plasma conductivity computed using the gas–chemistry model described in the previous sections. The rate equations for the heavy species densities and the electron temperature, given by Eqs. (4) and (10), respectively, are solved using a second–order forward–Euler time scheme. The 0D–circuit model (Eq. (19)) is solved using a second–order centered advance. All results to be presented are converged with respect to the simulation time step.

Example diode current and voltage waveforms from the experiments discussed in Ref. 2 are shown in Fig. 1. The voltage rises to a peak value of around 850 kV after about 55 ns and the current peaks about 35 ns later at around 742 kA. The diode voltage and current waveforms are used to represent the beam energy and current profiles, respectively. Analytical approximations to these profiles are used in our simulations since the voltage profile is noisy during the entire pulse and the current is noisy during the first few nanoseconds. The simulated voltage profile is approximated assuming a linear rise from 100 kV to 850 kV over 55 ns and then a linear decay back to 100 kV over the next 95 ns. A profile of the form $I_b(t) = I_{b0}[1 - \cos(\pi t/\tau_b)]/2$ with $\tau_b = 90$ ns and $I_{b0} = 742$ kA is used for the beam current. The current density is obtained assuming a 1–cm thick beam with a mean radius of 7 cm giving a peak current density of 16.9 kA/cm^2. The wall radius in these experiments is $r_w = 10$ cm.

It should be mentioned that although the gas is stated to be air in Ref. 2, that a closer look at the source of the data shows that only the low pressure shots ($P \le 0.12$ Torr) were in air. All of the experimental data presented in Ref. 2 for $0.5 \le P \le 10$ Torr, which is the pressure regime of interest here, were in nitrogen.
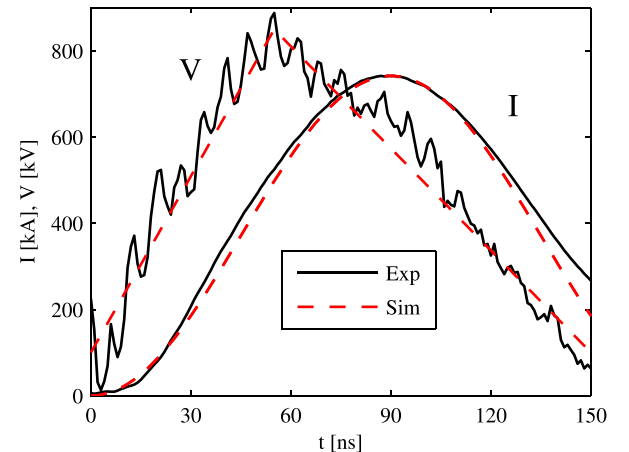

FIG. 1. Example diode voltage and current waveforms from GII experiments in Ref. 2. The dashed–red curves are analytical approximations to these profiles that are used in the simulations.

A. Simulation results for P = 1 Torr

The time variation of several important parameters from a simulation in 1–Torr nitrogen is shown in Fig. 2. The plasma conductivity is shown in the top left and the net current is shown in the bottom left. The conductivity rises to a value on the order of 10^{14} Hz near peak current and remains above 10^{13} Hz for the remainder of the pulse. This gives a characteristic L/R time of $1/\nu \approx 1\,\mu$s. The plasma return current is negligible during the first few nanoseconds and $I_{net} = I_b$ during this time. The net current becomes significantly different from I_b as the gas conductivity rises and the medium transitions from an insulator to a good conductor. The net current after breakdown is essentially frozen–in and has a weak variation in time compared to the beam current because the characteristic 1–μs L/R time after breakdown is much longer than the 150–ns beam pulse duration.

Also shown in Fig. 2 are the ionization fractions with respect to the total atom density $n_a = 2n_{N2}(t = 0)$ (top right) and the momentum exchange frequency (bottom right). Assuming the gas to be initially at room temperature, $n_a = 6.43 \times 10^{16}$/cm^3 for 1–Torr molecular nitrogen. These curves demonstrate the transition of the gas from a weakly ionized molecular state to a strongly ionized atomic state. The electron density rises to about 10% of n_a by peak current and continues to rise to about 45% near the end of the pulse. The molecular–ion density and atomic–ion density are also shown in this figure. The atomic ions make up the majority of the charge fraction after about 50 ns. The momentum–exchange frequency is more–or–less constant around 10^{10} Hz during the first 50 ns and is set by collisions with neutrals, but then steadily rises for $t > 50$ ns when momentum transfer is set by collisions with ions.

The decay of the molecular–ion species seen at the top right figure of Fig. 2 is a result of dissociative recombination, which occurs on the time scale of the beam pulse. The atomic–ion recombination mechanisms are too slow to take effect on these time scales and so the atomic ion density, and thus the electron density, hang up at the end of the pulse rather than decreasing. This time behavior is also observed in the line–integrated electron–density profiles measured with laser interferometry.[2] The peak electron density from the simulation is 2.9×10^{16}/cm^3. This value is in good agreement with the experimental results presented in Ref. 2 where line–integrated electron density measurements in 1–Torr nitrogen were measured to be $3 \times 10^{16} < n_eL < 6 \times 10^{16}$/cm^2 and the path length was about $L = 2$ cm.

The transition of the gas from a molecular to an atomic state is also illustrated in Fig. 3 where the densities of different molecular and atomic states are shown. Most of the molecules remain in the ground neutral state $N_2(X^1\Sigma)$, but the density drops about an order of magnitude by the end of the pulse. The atomic–species densities become comparable to the molecular densities at about 50 ns and are much larger than the molecular densities near the end of the pulse. The excited–atomic neutral population is mostly due to the metastable states $N(^2D^o)$ and $N(^2P^o)$. The net sum of the density of the high–lying optically allowed states is several orders–of–magnitude smaller than those of the metastable states. The density of ions with charge state greater than one is also negligible.

The reason n_e stops increasing near the end of the pulse is because the electron temperature decreases to a value of about 1 eV making further ionization energetically unfavorable. The falling temperature also produces a rising momentum-transfer frequency from Coulomb collisions, which varies as $T_e^{3/2}$, as seen in Fig. 2. The electron temperature from this simulation is shown in Fig. 4. T_e spikes to 24 eV during the first few nanoseconds, decays to below 10 eV after 10 ns, and continues to decay to about 1 eV at the end of the pulse. The large spike during the first few nanoseconds is a consequence of the large inductive electric field produced by the time–varying, un–neutralized beam current
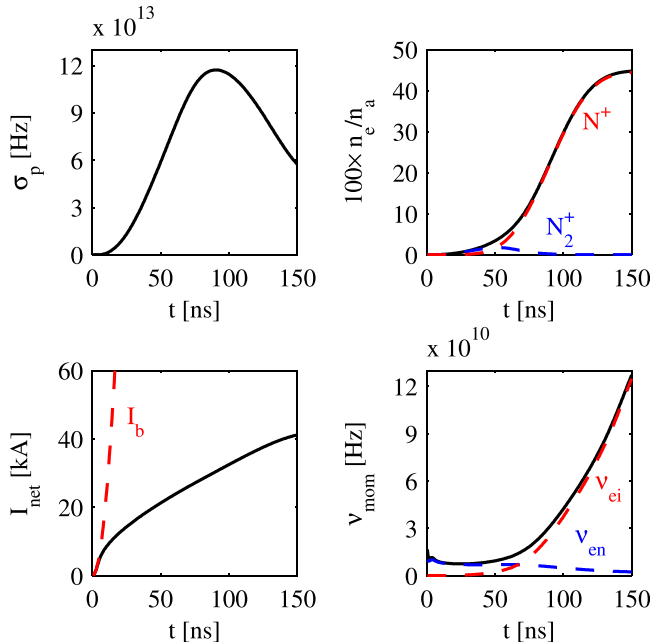

FIG. 2. Time evolution of plasma conductivity (top left), net current (bottom left), ionization fraction (top right), and momentum exchange frequency (bottom right) from 1 Torr simulation.
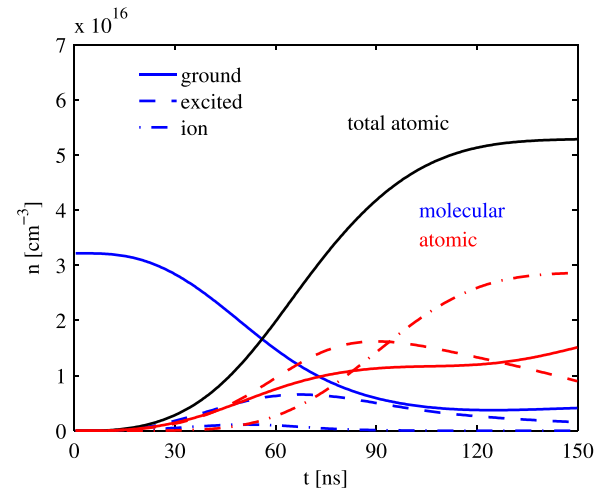

FIG. 3. Time evolution of heavy species densities from 1 Torr simulation. The blue curves are molecular species and the red curves are atomic species. The excited and ionic curves for both molecules and atomic species are the net sum of all such states.
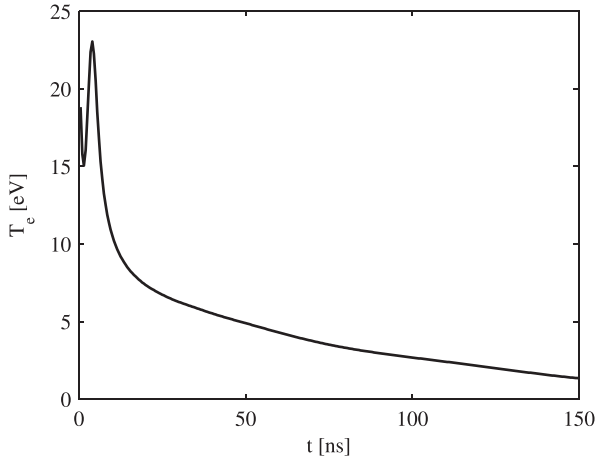
FIG. 4. Variation of electron temperature with time from the 1–Torr simulation.

before the gas breaks downs and generates a significant return current. Since this occurs during the weakly ionized stage of the pulse where momentum transfer is set by collisions with neutrals, then from power balance the electron temperature is a function of the reduced electric field E/N, where N is the neutral density and $E = L'_z dI_b/dt$. This is equivalent to the two–term solution,[11] where $T_e = T_e(E/N)$. The peak electric field value occurs at the same point as the peak temperature and has a value of 790 V/cm, which is below the runaway value in molecular nitrogen of about 1.25 kV/cm Torr.[51]

The electron–temperature evolution depends on the time–dependent rates of energy–density sources and sinks in Eq. (10). The decomposition of the energy–density sinks into contributions from different species is shown in Fig. 5. The sources of energy density, which are Joule heating

($P_J = \mathbf{J}_p \cdot \mathbf{E}$) and that from beam–impact processes (P_b), are also shown and it can be seen that the heating from beam–impact processes is negligible with respect to Ohmic heating. The energy–density sinks are dominated by inelastic processes with molecular species during the rise of the pulse and with atomic species during the latter half of the pulse. The losses are dominated by collisions with the ground electronic state $N_2(X^1\Sigma)$ during the molecular phase. During the atomic phase, collisions with the ground and metastable states of N control the energy–density sinks initially. However, near the end of the pulse, collisions with the ground and metastable states of N^+ are the largest energy–density sinks. Superelastic processes with N and N_2 actually become sources near the end of the pulse where T_e is low and quenching processes become important.

The electron temperature is seen in Fig. 4 to drop below 5 eV during the last 100 ns of the pulse. This is the temperature range were vibrational kinetics, which are ignored in this work, are typically important in determining the EEDF and contributing to the inelastic energy sink for the thermal electron species. However, since the gas is strongly ionized and mostly in an atomic state during this time where $T_e \lesssim 5$, vibrational kinetics are not expected to have a large effect on these results. Electron-electron relaxation will drive EEDF to a Maxwellian and inelastic processes with atomic species will set the energy sink (see Fig. 5).

An important part of quantifying the transition from a weakly ionized molecular state to a strongly ionized atomic state is to look at which processes dominate the production of electrons and atomic species during the pulse. Electron production rates from different processes are shown in the top figure of Fig. 6. Even though the population density of the high–lying optically allowed states of atomic nitrogen (red dashed–dashed curve) is much lower than those of the
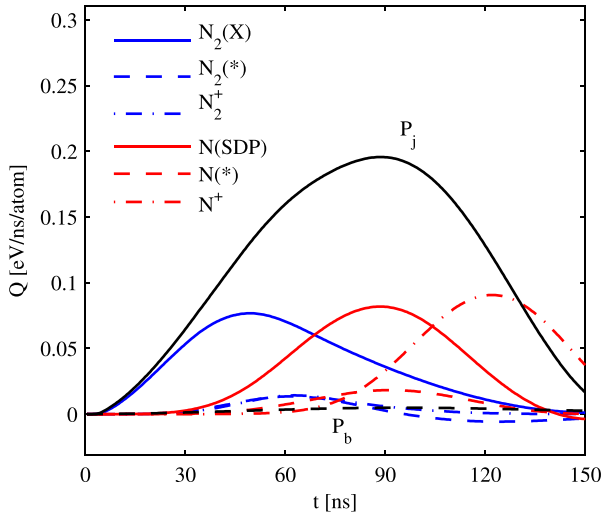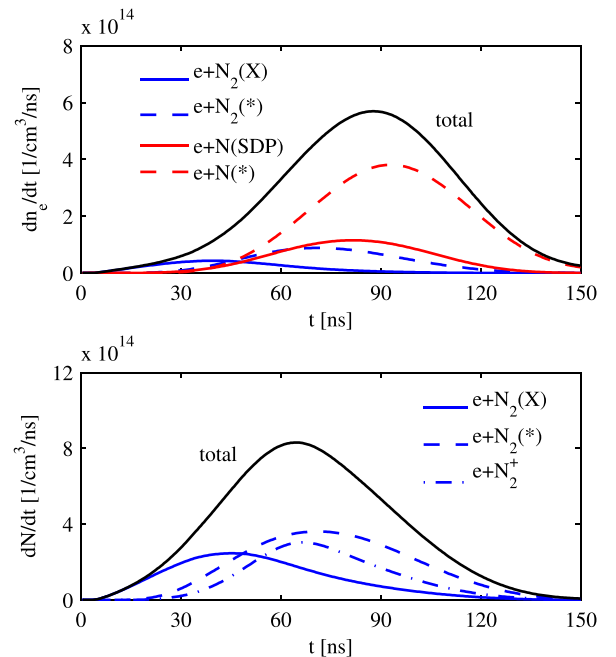

FIG. 5. Variation of electron power density components from the 1–Torr simulation. The Joule heating term is shown by the solid black line, and beam heating is shown by the dashed black line. Blue lines are for energy losses to molecular species and red are for energy losses to atomic species. The dashed blue line is energy lost due to collisions with all excited states of molecular nitrogen. The dashed red curve is energy lost due to collisions with the optically allowed neutral atomic states. The dashed–dotted curves represent losses due to collisions with ionic species.

FIG. 6. Thermal–ionization (top) and atomic–production (bottom) channels from 1–Torr simulation.

ground and metastable states (solid red curve), their contribution to the production of electrons are much larger. This is because they have energy levels within a few eV of the ionization limit[43] and so the cross sections for ionization from these states are much larger. Atomic species production rates from different processes are shown in the bottom figure of Fig. 6. Dissociation of ground state N_2 plays the dominant role for $t \lesssim 50$ ns. At later times, step–wise dissociation of the electronic states of molecular nitrogen and dissociative recombination of N_2^+ yield the largest contribution to the production of atomic nitrogen. Beam impact sources are included in the total rates shown in Fig. 6, but these rates are only relevant during the first few nanoseconds and are insignificant compared to thermal processes during the remainder of the pulse.

B. Radiative processes

Radiative transitions are ignored in the model based upon the assumption that electron–impact reactions dominate the system of rate equations. Many of the important radiative processes in both molecular and atomic nitrogen have lifetimes comparable to or shorter than the 150 ns time scales of interest. However, the system is optically thick to most of these lines making their effective lifetimes much longer. A detailed analysis of the time–dependent behavior of line–radiation intensity is beyond the scope of the present paper but is something that the Authors plan to consider in more detail in future work. Some comments and discussion concerning radiative processes are given below.

The relevant radiative transitions for the molecular species are the second positive system $N_2(C^3\Pi \rightarrow B^3\Pi) + h\nu$ and the first negative system $N_2^+(B^2\Sigma \rightarrow X^2\Sigma) + h\nu$. The effective Einstein coefficients (summed over the vibrational modes of the final electronic state) for the ground vibrational mode of these radiating electronic states are $A_{CB} = 2.7 \times 10^7$ Hz and $A_{BX} = 1.6 \times 10^7$ Hz, respectively.[30] Photons from the $(v', v'') = (0, 0)$ transitions of these processes have wavelengths of 337 nm and 391 nm for the second positive and the first negative system, respectively.

The relevant atomic transitions are given in Ref. 52. These transitions are too numerous to list, but in general they can be divided into two different groups—transitions from high–lying excited–energy states to the ground and metastable states and transitions from high–lying excited–energy states to lower high–lying excited–energy states. The former of these transition groups emits radiation with wavelengths below 180 nm, while the latter emits radiation at wavelengths above 680 nm.

The time evolution of some of the radiating states are shown in Fig. 7. The radiating neutral atomic states with the largest densities are the $N(3s\,^4P)$, $N(2p^4\,^4P)$, and $N(3p\,^4D^o)$ states. The $N(3s\,^4P)$ and $N(2p^4\,^4P)$ states both have strong transitions to the ground state with Einstein coefficients of 4.0×10^8 Hz and 1.5×10^8 Hz and wavelengths of 120 nm and 113 nm, respectively.[52] The $N(3p\,^4D^o)$ state has a strong transition to the $N(3s\,^4P)$ state with an Einstein coefficient of $A = 2.5 \times 10^7$ Hz and a wavelength of 869 nm.
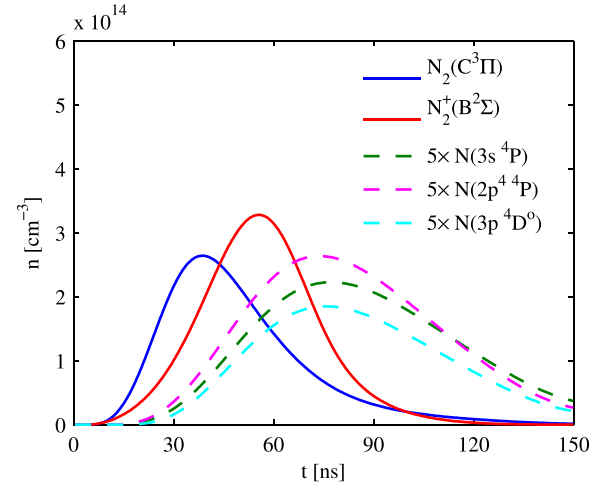

FIG. 7. Density profiles of some radiating states from the 1–Torr simulation. The densities of the atomic states are all scaled up by a factor of five.

Time profiles of the line radiation could be expected to follow the time profiles of the emitting densities if the system is optically thin. However, as mentioned above, the system is optically thick and a more detailed analysis that considers time–dependent escape factors[53] based on the optical mean free path of each line is needed for accurately predicting line-radiation profiles. For example, assuming that the line–broadening is only due to the Doppler effect,[54,55] then models for the neutral species temperature and densities of the absorbing states, which requires resolving the vibrational distribution of the molecular species, are needed to accurately calculate time–dependent escape factors.

The line–center cross section for pure Doppler broadening in units of 10^{-16} cm^2 can be expressed as $\sigma_\nu = f_{osc}\lambda\sqrt{M_h/T_h}$, where f_{osc} is the oscillator strength for the transition with wavelength λ in angstroms, M_h is the heavy species mass in atomic mass units, and T_h is the heavy species temperature in eV. Estimates of the heavy species temperature T_h based upon assuming elastic–energy transfer from electrons to the heavy species is the dominant heating mechanism show that T_h rises from room temperature at $t = 0$ to about 1 eV at $t = 150$ ns. The optical mean free paths for the transitions discussed above ($\lambda_{omfp} = 1/(n\sigma_\nu)$), where n is the density of the absorbing species) are all less than 1 mm using $T_h = 1$ eV, absorbing state densities at the time where the emitting state density peaks, and oscillator strengths from Ref. 52 for atomic transitions and from Ref. 56 for molecular transitions. The optical mean free paths for atomic transitions that terminate on the ground atomic state are actually on the order of 10 μm due to the relatively large density of the ground atomic state. The system can be considered optically thick to these lines since the 1–cm thickness of the plasma channel is much larger than the optical mean free path values.

C. Variation of results with maximum beam current density

For a given pulse duration and pressure, the main factor controlling the state of the gas is the beam current density. The state is controlled primarily by thermal–electron

reactions whose main energy source is Joule heating associated with the plasma return current, which, in turn, is approximately equal to the beam current density when current neutralization is high. Variation of the species densities at the end of a 150–ns pulse in 1–Torr nitrogen with maximum beam current density is shown in Fig. 8. The results in this figure are obtained by varying the magnitude of the beam current density with all other parameters the same as used for the 1–Torr simulation discussed in the Subsection IV B.

Three different regimes for a typical GII time pulse in 1–Torr nitrogen can be identified from Fig. 8. The neutral and ion species are mostly molecular for $J_{b0} \lesssim 3\,\mathrm{kA/cm^2}$. This is the weakly ionized molecular regime. For $3 \lesssim J_{b0} \lesssim 50\,\mathrm{kA/cm^2}$, the neutrals are mostly in an atomic state and the ions are mostly in the N^+ state. This is called the dissociated regime. The species are mostly higher–ionization states of atomic nitrogen for $J_{b0} \gtrsim 50\,\mathrm{kA/cm^2}$, which is called the coronal regime.[3] The model presented in this paper is most applicable in the dissociated regime. Non–Maxwellian EEDF's and a more detailed consideration of molecular processes, such as vibrational kinetics, should be considered in the weakly ionized, molecular regime. For the coronal regime, the role of high–lying optically allowed ion states may be important.

D. Variation of results with gas pressure

It is also of interest to understand how results vary with gas pressure. The simulation results presented in this section are obtained using the same parameters used for the 1–Torr simulations discussed previously and varying the pressure. The variation of the electron density at the end of the 150–ns pulse with pressures between 0.5 and 10 Torr is shown in the top figure of Fig. 9. The variation of the net current fraction with pressure at peak beam current ($t = 90\,\mathrm{ns}$) is shown in the bottom figure of Fig. 9. In these figures, results from our simulations (Sim) are compared with the GII experimental results in (Exp) and LSP simulations using its swarm model, both of which are presented in Ref. 2.

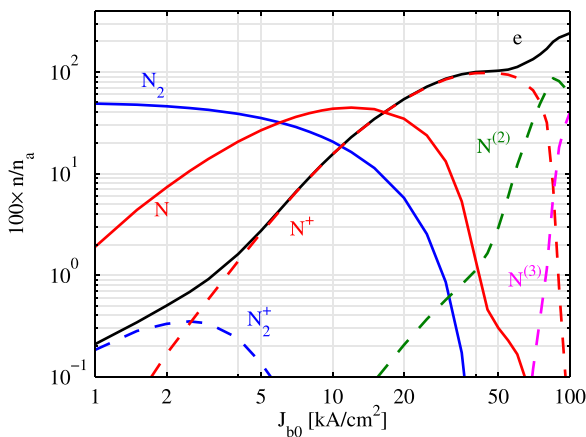The scaling of n_e with pressure from our simulations agrees qualitatively with the experimental measurements
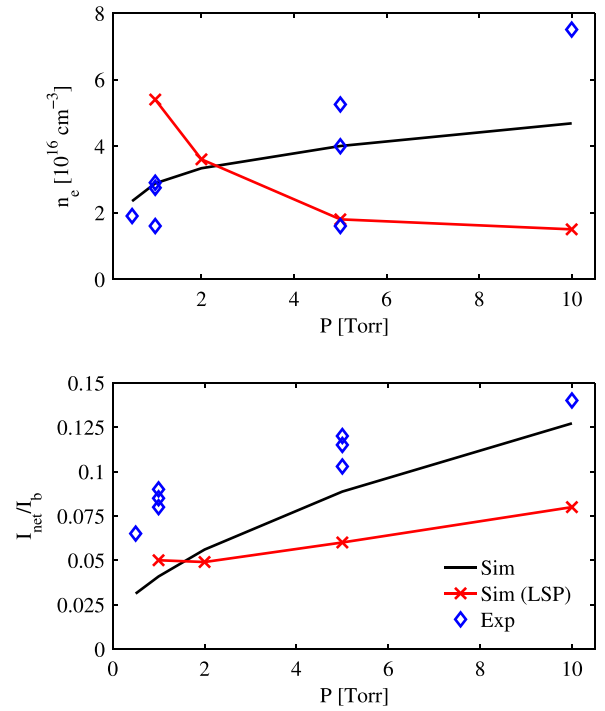

FIG. 9. Comparison of simulation (Sim) results at different pressures from 0D model with experimental results (Exp) and LSP simulations from Ref. 2. The electron density at the end of the 150 ns pulse in shown in the top figure and the net–current fraction at peak beam current is shown in the bottom figure.

shown in Ref. 2. The experimental values are inferred from the interferometry measurements of the line–integrated electron density assuming a path length of 2 cm. There is quite a bit of spread in the data—a factor of two at 1 Torr and a factor of three at 5 Torr—but the overall trend seems to be a modest increase in n_e with pressure in this range. The simulation results from the model presented in this paper captures the overall trend much better than the LSP simulations from Ref. 2, which show a decrease of n_e with increasing pressure. As discussed in the Introduction, the gas–chemistry model used in the simulations presented in Ref. 2 is based on the gas remaining molecular and weakly ionized. It should also be emphasized that the dissociative–recombination coefficient was set to zero in these simulations.

The increase in n_e with pressure from the simulations does not seem to be as strong as what is seen in the experiments. The agreement is good at 1 Torr and 5 Torr, but the results are off by about a factor of two at 10 Torr. The simulation results could be within the experimental error since there is only one experimental data point at this pressure. However, there is reason to believe that the 0D model will underestimate n_e at higher pressures. This can be understood by looking at the variation of the net–current fraction, $f = I_{\mathrm{net}}/I_b$, at peak beam current ($I_b(t = 90\mathrm{ns}) = 742$ kA) with pressure shown in the bottom figure of Fig. 9. The simulation and experiments both show an increase in f with pressure in this pressure range. An increase in the net current could cause the beam to pinch more strongly at higher pressures and thus the current density of the beam would increase.[3] Since n_e has a nonlinear dependence with current density (see Fig. 8), this may explain the stronger increase in

FIG. 8. Distribution of species density fractions at end of pulse with maximum beam current density in 1–Torr nitrogen. The N_2 curve contains all N_2 species and similarly for all other species.

n_e seen experimentally in comparison to that found from the 0D model, which assumes a rigid beam.

Similar to the electron density variation with pressure, the net–current fraction increases with pressure. The overall trend of this increase is also seen in the simulation results, which are much improved over the LSP simulations presented previously. In contrast to the electron density variation with pressure, the simulation agreement is best at 10 Torr and about a factor of two or three low at 1 Torr. However, since the background plasma is driven by Joule heating, the beam current is the most important parameter for modeling the background plasma. Since $f \ll 1$ in both the simulation and experiments, then the simulated plasma current is in excellent agreement with plasma current in the experiments.

E. Reduced species model (RSM)

Reduced models with a minimal number of states are more practical for coupling gas–chemistry models to PIC codes for self–consistent beam–transport studies. A comparison of some results obtained from a reduced species model (RSM) with the full model (FM) is shown in Fig. 10. The RSM neglects all of the optically allowed neutral–atomic states. With respect to the FM, it is seen that the electron density from the RSM is slightly lower near the end of the pulse and the electron temperature is slightly higher. This gives a conductivity from the RSM that is about 50% larger near the end of the pulse, but the net current profiles from the two models are practically identical since the system is a good conductor on these time scales and is therefore not sensitive to the conductivity.

It was shown previously in Fig. 6 that most of the ionization from the FM is due to thermal processes with the optically allowed states, which are ignored in the RSM. One might then expect that by neglecting these species that the

ionization fraction would go down significantly. However, by neglecting these species, the energy sink due to exciting these species is also neglected and the temperature in the RSM model is increased. This increase in temperature causes the ionization from the ground and metastable states to increase mediating some of the ionization lost by neglecting the optically allowed states.

V. DISCUSSION AND CONCLUSIONS

A detailed gas–chemistry model is presented in this paper for a dynamical description of moderate–pressure nitrogen plasmas produced by high–current–density electron beams generated by order 100–ns pulsed–power devices. The pressure regimes of interest are order 1 Torr and the current densities of interest are order $10 \, \text{kA/cm}^2$. For these parameter regimes, the gas transitions from a weakly ionized molecular state to a strongly ionized atomic state on the time scale of the beam pulse. Using the rigid–beam approximation, along with several other simplifying assumptions, the gas–chemistry model is coupled to a 0D–circuit model representative of a pulsed, annular electron beam transporting in a nitrogen–filled conducting cell. Results are presented from a simulation of a typical 150–ns GII beam with a peak current density of $16.9 \, \text{kA/cm}^2$ in 1–Torr nitrogen. The transition of the gas from a weakly ionized molecular state to a strongly ionized atomic state is illustrated in detail by analyzing the evolution of different species and by showing time profiles of the contribution of different species to momentum transfer, energy transfer, electron production, and atomic production.

One of the findings is that while most of the species are in the ground and metastable states of atomic neutral and singly ionized nitrogen during most of the pulse, the major contribution to the production of electrons comes from thermal ionization of the optically allowed neutral states of atomic nitrogen with excitation energies close to the ionization limit. Similarly, the largest contribution to atomic production comes from step–wise dissociation of the electronically excited states of N_2 and through dissociative recombination of N_2^+.

Both the time–profile and the magnitude of the electron density predicted by the 1–Torr simulation are in good agreement with n_e inferred from interferometry measurements. The scaling of the peak electron density with pressure from about 1–10 Torr is also in qualitative agreement with experimental measurements showing a modest increase of n_e with pressure in this range. The scaling of the net–current fraction with pressure from experiments also shows a modest increase with pressure in this pressure range. The simulation results show the same trend, but the magnitude is off by about a factor of two–to–three at 1 Torr. Preliminary data from more recent GII experiments using a similar diode show lower net–current fractions at 1 Torr than those from Ref. 2. In any case, disagreement with modeling could be a result of the oversimplification of the 0D model. These issues will be investigated in future experiments and future simulations.
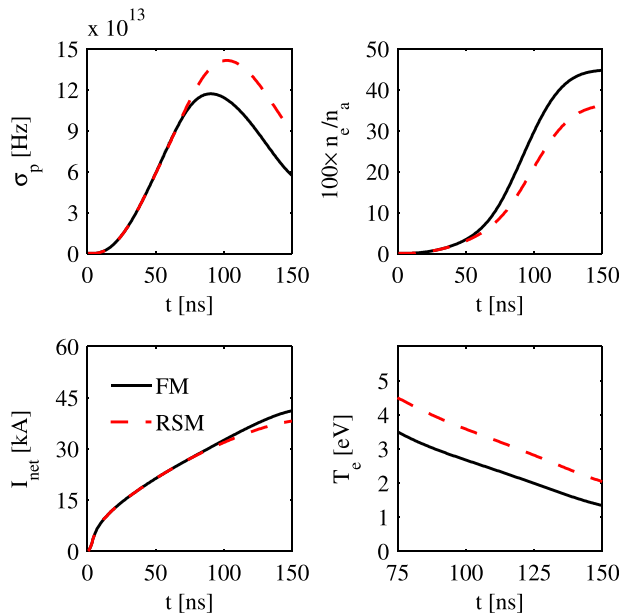

FIG. 10. Comparison of results found using a reduced species model (RSM) with the full model (FM). The conductivity, percent ionization, net current, and electron temperature are shown in the figures located in top left, top right, bottom left, and bottom right, respectively.

The purpose of this manuscript is to give a dynamical description of the nitrogen plasmas produced during a typical electron beam shot on GII. To this end, a 0D circuit model derived under the rigid–beam approximation suffices. Good qualitative agreement with experiments is obtained, but a quantitative analysis requires self–consistent calculations of the gas–chemistry along with the spatially dependent electric and magnetic fields and the beam–electron trajectories. Previous work has demonstrated the importance of some of these non–0D effects when trying to compare with experiments.[3,8] For example, interferometry measures the line integrated electron density across the beam axis. Due to the nonlinear dependence of the local density with the beam current density (see Fig. 8), self–consistent beam orbits that account for beam scatter due to anode foils and magnetic pinching, both of which can alter the current density, may be important. In future work, the model presented in this paper will be coupled with a PIC model to perform self–consistent hybrid 2D simulations and a more detailed comparison with experimental results will be presented.

The gas–chemistry model used in this work is for a specific set of parameter regimes where many simplifying assumptions are justified. Additional physics that may become important outside the parameter regimes of interest are worth discussing. For peak current densities below $10 \, \mathrm{kA/cm}^2$ and for pressures higher than 10 Torr, more details of weakly ionized gases, such as non–Maxwellian EEDF's, and more details of molecular physics, such as vibrational kinetics, should be considered. Non–Maxwellian features may also be important for all parameter regimes early in time when electron–neutral collisions with $N_2(X^1\Sigma)$ set the EEDF and on time scales longer than the pulse duration where superelastic collisions with excited states can superimpose structures on the EEDF.[57] There are many complicating factors that need to be considered for pressures significantly lower than 1 Torr. This includes non–local effects due to the increased mean free path of the secondaries produced by beam–impact ionization, electron runaway[10] due to the large reduced electric fields that arise before breakdown occurs, effects of strong magnetic fields[58] ($\Omega > \nu_{\mathrm{mom}}$) due to poor currently neutralization,[2] and anomalous resistivity due to the two–stream instability that can occur when $\mathbf{V}_e > \sqrt{T_e/m_e}$.[59]

ACKNOWLEDGMENTS

[1]J. Bretagne, G. Delouya, and V. Puech, J. Phys. D: Appl. Phys. **14**, 1225 (1981).
[2]S. Strasburg, D. D. Hinshelwood, J. W. Schumer, D. Mosher, P. F. Ottinger, R. F. Fernsler, and S. P. Slinker, Phys. Plasmas **10**, 3758 (2003).
[3]S. Strasburg, D. D. Hinshelwood, J. W. Schumer, D. Mosher, and P. F. Ottinger, in *Proceedings of the 14th IEEE International Pulsed Power Conference* (2003), p. 991.
[4]G. M. Petrov, D. R. Boris, T. B. Petrova, E. H. Lock, R. F. Fernsler, and S. G. Walton, Plasma Sources Sci. Technol. **22**, 065005 (2013).
[5]T. W. L. Sanford, Phys. Plasmas **2**, 2539 (1995).
[6]J. Shipman, IEEE Trans. Nucl. Sci. **18**, 243 (1971).
[7]R. B. Miller, *An Introduction to the Physics of Intense Charged Particle Beams* (Plenum Press, New York and London, 1982).
[8]D. A. McArthur and J. W. Poukey, Phys. Rev. Lett. **27**, 1765 (1971).
[9]D. A. McArthur and J. W. Poukey, Phys. Fluids **16**, 1996 (1973).
[10]D. R. Welch, C. L. Olson, and T. W. L. Sanford, Phys. Plasmas **1**, 764 (1994).
[11]G. J. M. Hagelaar and L. C. Pitchford, Plasma Sources Sci. Technol. **14**, 722 (2005).
[12]D. V. Rose, D. R. Welch, P. F. Ottinger, and J. W. Schumer, Phys. Plasmas **8**, 4972 (2001).
[13]S. Strasburg, D. D. Hinshelwood, P. F. Ottinger, J. W. Schumer, R. Commisso, S. Stephanakis, V. Chorny, and D. V. Rose, Phys. Plasmas **10**, 2527 (2003).
[14]D. R. Welch, D. V. Rose, B. V. Oliver, E. Schamiloglu, K. Hahn, and J. E. Maenchen, Phys. Plasmas **11**, 751 (2004).
[15]D. R. Welch, R. Clark, D. V. Rose, C. Thoma, T. C. Genoni, N. Bruner, and T. P. Hughes, *Algorithms for Hybrid Simulation*, Technical Report No. VSL-0726, Voss Scientific, 2007.
[16]Y. Itikawa, J. Phys. Chem. Ref. Data **35**, 31 (2006).
[17]E. Zipf and R. McLaughlin, Planet. Space Sci. **26**, 449 (1978).
[18]A. Ali, *Electron Energy Loss Rates in N_2, O_2 and Air*, Technical Report (DTIC Document, 1984).
[19]A. V. Phelps and L. C. Pitchford, Phys. Rev. A **31**, 2932 (1985).
[20]E. Zipf, P. Espy, and C. Boyle, J. Geophys. Res. **85**, 687, doi:10.1029/JA085iA02p00687 (1980).
[21]J. Bacri and A. Medani, Phys. B + C **101**, 399 (1980).
[22]P. Teulet, J. Sarrette, and A. Gomes, J. Quant. Spectrosc. Radiat. Transfer **62**, 549 (1999).
[23]R. R. Laher and F. R. Gilmore, J. Phys. Chem. Ref. Data **20**, 685 (1991).
[24]F. R. Gilmore, J. Quant. Spectrosc. Radiat. Transfer **5**, 369 (1965).
[25]J. Loureiro and C. M. Ferreira, J. Phys. D: Appl. Phys. **19**, 17 (1986).
[26]G. Colonna and M. Capitelli, J. Thermophys. Heat Transfer **10**, 406 (1996).
[27]K. Vereshchagin, V. Smirnov, and V. Shakhatov, Tech. Phys. **42**, 487 (1997).
[28]M. Capitelli, G. Colonna, G. D'Ammando, V. Laporta, and A. Laricchiuta, Phys. Plasmas **20**, 101609 (2013).
[29]A. Kosarim, B. Smirnov, M. Capitelli, R. Celiberto, G. Petrella, and A. Laricchiuta, Chem. Phys. Lett. **414**, 215 (2005).
[30]F. R. Gilmore, R. R. Laher, and P. J. Espy, J. Phys. Chem. Ref. Data **21**, 1005 (1992).
[31]P. B. Armentrout, S. M. Tarr, A. Dori, and R. S. Freund, J. Chem. Phys. **75**, 2786 (1981).
[32]J. R. Peterson, A. Le Padellec, H. Danared, G. H. Dunn, M. Larsson, A. Larson, R. Peverall, C. Strömholm, S. Rosén, M. af Ugglas, and W. J. van der Zande, J. Chem. Phys. **108**, 1978 (1998).
[33]M. A. Lieberman and A. J. Lichtenberg, *Principles of Plasma Discharges and Material Processing*, 2nd ed. (John Wiley and Sons, Inc., 2005), p. 245.
[34]R. McWhirter, *Spectral Intensities in Plasma Diagnostic Techniques* (Academic Press, New York, 1965).
[35]Y. Wang, O. Zatsarinny, and K. Bartschat, Phys. Rev. A **89**, 062714 (2014).
[36]K. A. Berrington, P. G. Burke, and W. D. Robb, J. Phys. B: At. Mol. Phys. **8**, 2500 (1975).
[37]R. J. W. Henry, P. G. Burke, and A.-L. Sinfailam, Phys. Rev. **178**, 218 (1969).
[38]R. D. Taylor, S. P. Slinker, and A. W. Ali, J. Appl. Phys. **64**, 982 (1988).
[39]Y.-K. Kim and J.-P. Desclaux, Phys. Rev. A **66**, 012708 (2002).
[40]E. Brook, M. Harrison, and A. Smith, J. Phys. B: At. Mol. Phys. **11**, 3115 (1978).
[41]W. Lotz, Z. Phys. **206**, 205 (1967).
[42]W. Lotz, Z. Phys. **216**, 241 (1968).
[43]W. M. Huo, VKI LS Nonequilibrium gas dynamics from physical models to hypersonic flights, Rhode-Saint-Genese, Belgium, 2008.
[44]S. P. Slinker, A. W. Ali, and R. D. Taylor, J. Appl. Phys. **67**, 679 (1990).
[45]H. Bethe, *Handbook of Physics* (Springer, Berlin, 1933), Vol. 24, p. 273.
[46]Y. B. Zeldovich and Y. P. Raizer, *Physics of Shock Waves and High-Temperature Plasmas* (Academic Press, New York, 1966), Vol. I.
[47]L. J. M. Ignjatović and A. A. Mihajlov, Contrib. Plasma Phys. **37**, 309 (1997).
[48]M. Capitelli, D. Bruno, and A. Laricchiuta, Transport **74**, 165–204 (2013).

[49]L. Spitzer and R. Härm, Phys. Rev. **89**, 977 (1953).
[50]M. A. Greenspan and R. E. Juhala, J. Appl. Phys. **57**, 67 (1985).
[51]J. Lidestri, P. Spence, V. Bailey, S. Putnam, J. Fockler, C. Eichenberger, and P. Champney, IEEE Trans. Plasma Sci. **19**, 855 (1991).
[52]W. L. Wiese and J. R. Fuhr, J. Phys. Chem. Ref. Data **36**, 1287 (2007).
[53]T. Holstein, Phys. Rev. **72**, 1212 (1947).
[54]A. Bultel, B. G. Chéron, A. Bourdon, O. Motapon, and I. F. Schneider, Phys. Plasmas **13**, 043502 (2006).
[55]J. Annaloro, A. Bultel, and P. Omaly, J. Thermophys. Heat Transfer **28**, 608 (2014).
[56]C. O. Laux and C. H. Kruger, J. Quant. Spectrosc. Radiat. Transfer **48**, 9 (1992).
[57]G. Colonna, G. D'Ammando, L. D. Pietanza, and M. Capitelli, Plasma Phys. Controlled Fusion **57**, 014009 (2015).
[58]S. Braginskii, Rev. Plasma Phys. **1**, 205 (1965).
[59]O. Buneman, Phys. Rev. **115**, 503 (1959).